Supplementary Materials for

Plume-Induced Flood Basalts on Hesperian Mars: An Investigation of Hesperia Planum

A. Broquet*, J. C. Andrews-Hanna

Correspondence to: adrienbroquet@email.arizona.edu

This PDF file includes:

Supplementary Text

S1. Plume head size.

Several parameters influence the diameter of a plume head in the mantle (D), including the rise height through the mantle (Z), the kinematic viscosity (v), and the gravitational attraction (g), which all are expected to differ between the Earth and Mars, where (Campbell & Griffiths, 1990; Griffiths & Campbell 1991) $D \sim Z^{3/5}(v/g)^{1/5}$.

On Earth, plume heads are predicted to have diameters ranging from 1000–1200 km in the mantle (with a viscosity of 10^{20} Pa s), and flatten at the base of the lithosphere to reach diameters of 2000–2400 km (Griffiths & Campbell, 1991; White & McKenzie, 1995). On Mars, constraints on the Hesperian mantle viscosity are scarce and we assume a large range of viscosities from $10^{19–21}$ Pa s (Plesa et al., 2018). For a plume coming from the core-mantle boundary, plume heads would have diameters of 530 to 1600 km in the mantle, and 1060 to 3200 km after flattening. Our model results with a flattened plume head diameter of 1400 km are thus consistent with expected plume head sizes on Mars.

S2. An updated thin-shell model for displacement and strain calculations.

The thin-shell formalism used in this study is based on the initial formulation of Banerdt (1986) and can be found at Broquet (2022). Various improvements have been made to the initial formulation to include finite-amplitude correction and filtering (Wieczorek & Phillips, 1998), but also lateral density variations at any arbitrary depth (Wieczorek et al., 2013). Some corrections have been made to the model and are noted below.

The model solves a system of 5 equations that links 8 parameters expressed in spherical harmonics (degree l, order m): the topography (H_{lm}), geoid at the surface of the planet (G_{lm}), geoid at the base of the crust (Gc_{lm}), net acting load on the lithosphere (q_{lm}), tangential load potential (Ω_{lm}), flexure of the lithosphere (w_{lm}), crustal root variations (δc_{lm}), and internal lateral density variations ($\delta\rho_{lm}$). Given 3 constraints or assumptions, the system is evenly determined. To simplify the following equations, the mass-sheet approximation is used (see Wieczorek et al., 2013 and Broquet 2022 for more details).

The net load acting on the lithosphere can be shown to be equal to (e.g., Broquet & Wieczorek, 2019)

$$q_{lm} = g_0\rho_c(H_{lm} - G_{lm}) + g_m\Delta\rho(w_{lm} - \delta c_{lm} - Gc_{lm}) + g_M\delta\rho_{lm}M \quad \text{(A1)}$$

where $\Delta\rho = \rho_m - \rho_c$ is the density contrast across the crust-mantle interface; g_0, g_m, and g_M are the vertical gravitational acceleration at the surface, crust-mantle boundary and at the base of the internal load; and M is the thickness of the internal density anomaly. If the gravitational acceleration is assumed to be constant, our equation (A1) reduces to eq. (4) in Banerdt (1986). Assuming that internal density variations are located between M_t and M_b, and using the mass-sheet assumption, the geoid at the surface can be derived as (see also Wieczorek & Phillips, 1998),

$$G_{lm} = \frac{3}{\bar{\rho}(2l+1)} \left\{ \rho_c H_{lm} + \Delta\rho(w_{lm} - \delta c_{lm})\varphi^{l+2} + \delta c_{lm} \frac{R}{l+3} \left[\left(\frac{R - M_t}{R} \right)^{l+3} - \left(\frac{R - M_b}{R} \right)^{l+3} \right] \right\}.$$

(A2)

In this equation, $\varphi = (R - T_c)/R$. Similarly, the geoid at the base of the crust is given by

$$Gc_{lm} = \frac{3}{\bar{\rho}(2l+1)} \left\{ \rho_c H_{lm} \varphi^{l+1} + \Delta\rho(w_{lm} - \delta c_{lm})\varphi^3 + \delta c_{lm} \frac{R}{l+3} \left[\frac{\left(\frac{R - T_c}{R - M_t} \right)^{l+1} - (R - M_t)^3}{(R - T_c)R^2} - \frac{\left(\frac{R - T_c}{R - M_b} \right)^{l+1} - (R - M_b)^3}{(R - T_c)R^2} \right] \right\},$$

(A3)

Equation (A2) is similar to eq. (6) in Banerdt (1986), and minor corrections have been made to equation (A3), with respect to eq. (5) in Banerdt (1986), to properly reference the different interfaces at the base of the crust.

The tangential load potential has been derived by Banerdt (1986) as

$$\Omega_{lm} = \frac{v}{1-v} \rho_c g_0 T_e \frac{H_{lm}}{R} - \left[\rho_c g_m \left(\frac{v}{1-v} T_e - T_c \right) - \rho_m g_m max(T_e - T_c, 0) \right] \frac{w_{lm}}{R} - \frac{v}{1-v} \Delta\rho g_m max(T_e - T_c, 0) \frac{\delta c_{lm}}{R} - \frac{1}{2} \frac{v}{1-v} \delta\rho_{lm} g_m max(T_e - M_t, 0) \frac{min(M, T_e - M_t)}{R}.$$

(A4)

Equation (A4) has been modified to include lateral density variations at any arbitrary depth. We note that any internal density variations below the elastic lithosphere do not give rise to tangential loads, as these are assumed to be in the fluid mantle.

The flexure equation is obtained from Beuthe (2008)

$$w_{lm} = \frac{-R_e^4(\nabla + 1 - v)q_{lm} + R_e^4 \left(\frac{1}{1+\xi}(\nabla + 2) - 1 - v \right) \nabla\Omega_{lm}}{\eta D \nabla(\nabla + 2)^2 + \frac{R_e^2}{ET_e}(\nabla + 2)}$$

(A5)

where, $\nabla = -l(l+1)$ is the Laplacian, $D = ET_e^3/(12(1-v^2))$ is the bending rigidity of the shell, $\xi = 12R_e^2/T_e^2$, and $\eta = \xi/(1 + \xi)$. The flexure equation is slightly different from that derived in Banerdt (1986), with a correction that mostly affects the degree-1 terms (see Beuthe 2008).

Strains are computed using the flexure and the poloidal component of the tangential displacement, which is defined following Beuthe (2008) as

$$A_{lm} = \frac{1}{(1+\xi)(1-v^2)}(\nabla + 1 + v)(\nabla + 2)w_{lm} + w_{lm} + \frac{R_e^2 q_{lm}}{ET_e} - \frac{R_e^2}{(1+\xi)ET_e}\big(\nabla - \xi(1+v)\big)\Omega_{lm}$$

(A6)

From equations (A5) and (A6), one can derive the 6 components of the strain tensor (e.g., eq. 12 in Beuthe, 2008).

S3. Fitting the strain magnitude at Hesperia Planum.

We make use of the best-fit plume location and determine what parameters best reproduce the observed strain magnitude. To facilitate viewing the three-dimensional parameter space, we have fixed one parameter for each panel of Figure S2. We estimate a residual strain as the difference between the observed and predicted areal strain, both averaged over our restricted investigated region. Where the model best matches observations, the residual strain should be approximately $1.47–1.76\times10^{-3}$, which is the strain attributed to global contraction (section 3.3 in the main text).

In our models, there is roughly a one-to-one tradeoff between the density contrast and aspect ratio of the plume head (Figure S2A), which both control the mass and load of the plume. Decreasing the elastic thickness increases the residual strain (S2B), which is the result of our loading model approaching isostatic equilibrium ($T_e = 0$), where stresses and strains are minimum.

In order to best reproduce the observed strain magnitude and when flood lava loading is negligible, the plume-head density contrast should be at least -25 kg m^{-3} (thermal anomaly of about 215 K), the aspect ratio must be greater than 0.11, and any elastic thickness can satisfy the data. When accounting for the presence of the flood basalt, with an initial thickness of 500 m, less strain should originate from the plume-head. The density contrast and aspect ratio are both reduced, with minimum allowed values down to -10 kg m^{-3} and 0.09, respectively (Figure S2).

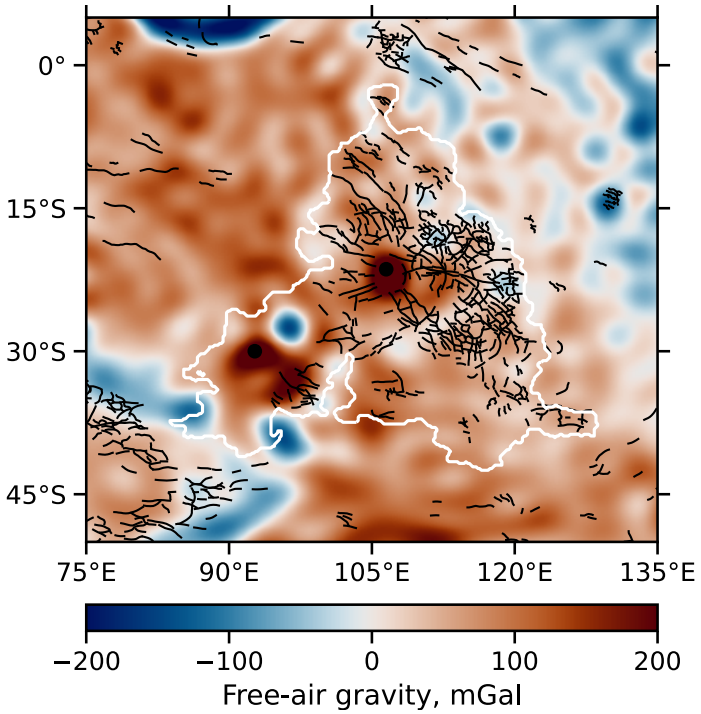

Figure S1: Gravity field at Hesperia Planum. Free-air gravity at Hesperia Planum based on the model of Genova et al. (2016). For geologic context, the images are annotated with a white contour of Hesperia Planum, black lines for compressive tectonic features and black dots for Tyrrhena (106°E -21°N) and Hadriaca (93°E -30°N) Montes.

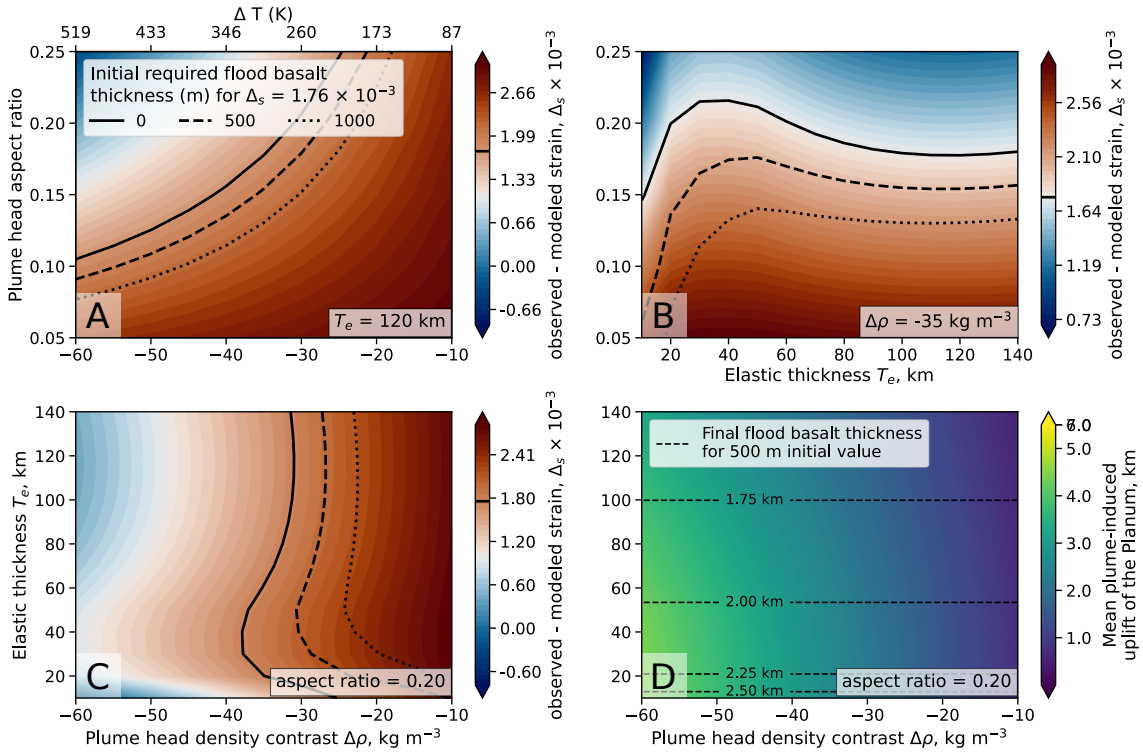

Figure S2: Strain magnitude and displacement at Hesperia Planum. (**A**) Residual strain (the difference between the observed strain of 3.20×10^{-3} and modeled areal strain) as a function of the density contrast (or temperature anomaly) and aspect ratio for an elastic thickness of 120 km. (**B**) Residual strain for different elastic and plume-head thicknesses for a density contrast of -35 kg m^{-3}. (**C**) Residual strain as a function of the density contrast and elastic thickness for an aspect ratio of 0.20. Black contours indicate where the residual strain is 1.76×10^{-3}, which is our estimate for the background Hesperian strain, for several initial thicknesses of the flood basalt. (**D**) Maximum predicted surface uplift for different elastic thickness and plume-head density contrast for an aspect ratio of 0.20. This plot is also annotated by the final flood basalt thickness depending on the elastic thickness and for an initial thickness of 500 m.

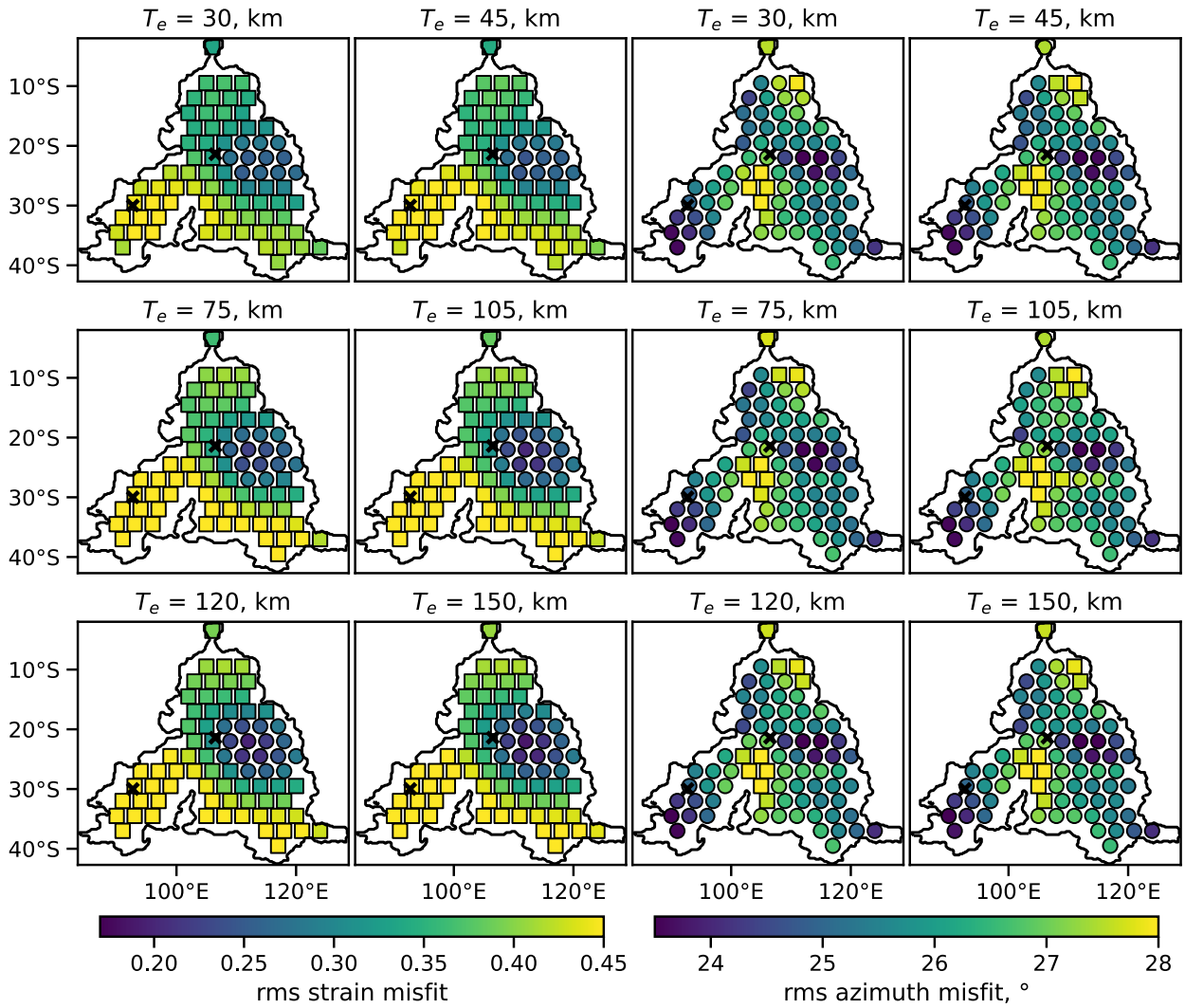

Figure S3: Mantle plume position and elastic thickness. Influence of the thickness of the elastic lithosphere on the RMS misfit between the observed and modeled strain concentration (2 leftmost columns) and azimuth (2 rightmost columns) as a function of the position the plume-head (colored markers). The plume-head radius, density, and aspect ratio were set to 700 km, -35 kg m^{-3}, and 0.20 respectively. Where the RMS misfit is lower than when using global gravity and topography (0.29) the location markers are dots, and are squares elsewhere. The black cross indicates the position of Tyrrhena and Hadriaca Montes.

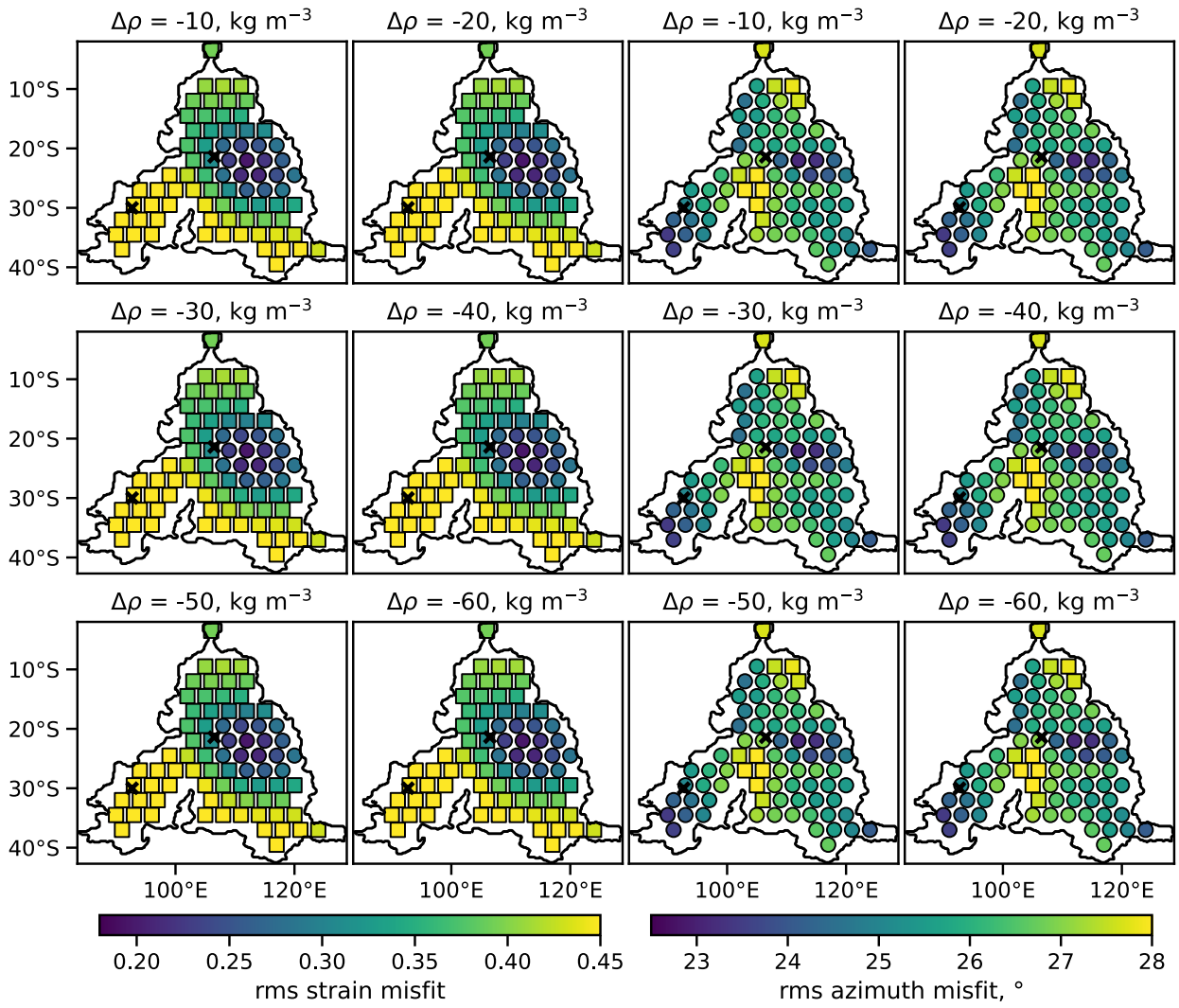

Figure S4: Mantle plume position and density contrast of the plume-head. Influence of the density contrast of the plume-head on the RMS misfit between the observed and modeled strain concentration (2 leftmost columns) and azimuth (2 rightmost columns) as a function of the position the plume-head (colored markers). The elastic thickness, plume-head radius and aspect ratio were set to 120 km, 700 km, and 0.20 respectively.

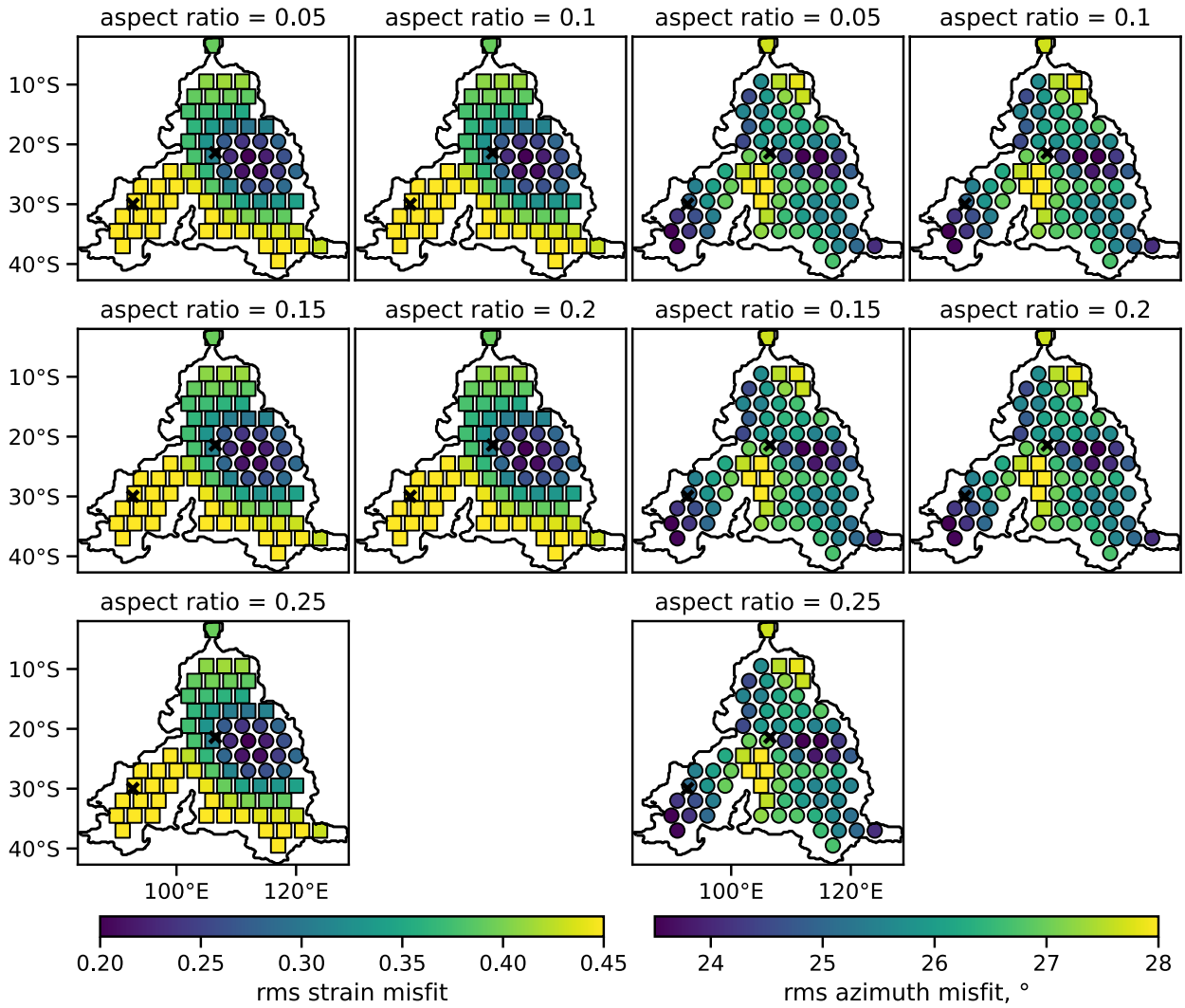

Figure S5: Mantle plume position and the aspect ratio of the plume-head. Influence of the aspect ratio of the plume-head on the RMS misfit between the observed and modeled strain concentration (2 leftmost columns) and azimuth (2 rightmost columns) as a function of the position the plume-head (colored markers). The elastic thickness, plume-head radius and density contrast were set to 120 km, 700 km, and -35 kg m^{-3}, respectively.

References

Banerdt, W. B. (1986). Support of long-wavelength loads on Venus and implications for internal structure. *Journal of Geophysical Research: Solid Earth*, *91*, 403– 419. https://doi.org/10.1029/JB091iB01p00403.

Broquet, A. (2022). AB-Ares/Displacement strain planet: Version 0.4.0. *Zenodo*. https://doi.org/10.5281/zenodo.5784417.

Beuthe, M. (2008). Thin elastic shells with variable thickness for lithospheric flexure of one-plate planets. *Geophysical Journal International*, *172*(2), 817–841. https://doi.org/10.1111/j.1365-246X.2007.03671.x.

Broquet, A., & Wieczorek, M. A. (2019). The gravitational signature of Martian volcanoes. *Journal of Geophysical Research: Planets*, *124*(8), 2054–2086. https://doi.org/10 .1029/2019JE005959.

Campbell, I. H., & Griffiths, R. W. (1990). Implications of mantle plume structure for the evolution of flood basalts. *Earth and Planetary Science Letters, 99*(1), 79–93. https://doi.org/10.1016/0012-821X(90)90072-6.

Genova, A., Goossens, S., Lemoine, F. G., Mazarico, E., Neumann, G. A., Smith, D. E., & Zuber, M. T. (2016). Seasonal and static gravity field of Mars from MGS, Mars Odyssey and MRO radio science. *Icarus*, *272*, 228–245. https://doi.org/10.1016/j.Icarus.2016.02.050.

Griffiths, R. W., & Campbell, I. H. (1991). Interaction of mantle plume heads with the Earth's surface and onset of small-scale convection. *Journal of Geophysical*

Research: Solid Earth, 96(B11), 18295–18310. https://doi.org/10.1029/91JB01897.

Plesa, A.-C., Padovan, S., Tosi, N., Breuer, D., Grott, M., Wieczorek, M. A., Spohn, T., Smrekar, S. E., & Banerdt, W. B. (2018). The thermal state and interior structure of Mars. *Geophysical Research Letters, 45*(22), 12,198–12,209. https://doi.org/10.1029/2018GL080728.

White, R. S., & McKenzie, D. (1995). Mantle plumes and flood basalts. *Journal of Geophysical Research: Solid Earth, 100*(B9), 17543–17585. https://doi.org/10.1029/ 95JB01585.

Wieczorek, M. A., Neumann, G. A., Nimmo, F., Kiefer, W. S., Jeffrey, T. G., Melosh, H. J., Phillips, R. J., Solomon, S. C., Andrews-Hanna, J. C., Asmar, S. W., Konopliv, A. S., Lemoine, F. G., Smith, D. E., Watkins, M. M., Williams, J. G., & Zuber, M. T. (2013). The crust of the Moon as seen by GRAIL. *Science*, *339*(6120), 671–675. https://doi.org/10.1126/science.1231530.

Wieczorek, M. A., & Phillips, R. J. (1998). Potential anomalies on a sphere: Applications to the thickness of the lunar crust. *Journal of Geophysical Research: Planets*, *103*(E1), 1715–1724. https://doi.org/10.1029/97JE03136.